

Supporting Information: Origin, Evolution, and Movement of Microlayer in Pool Boiling

An Zou, Manish Gupta, Shalabh C. Maroo*

Department of Mechanical Engineering and Aerospace Engineering, Syracuse University, Syracuse, NY 13244

*Corresponding author: scmaroo@syr.edu

S1. Molecular Dynamics Simulation

LAMMPS is used to perform the MD simulations. The simulation domain consists of 22400 liquid argon atoms in between parallel solid walls with initial volume of 10.12nm x 10.28nm x 10nm. The wall atoms are arranged in fixed FCC (1, 1, 1) lattice structure. The upper wall has platinum atoms, while the lower wall has long range hydrophilic atoms. The effect of hydrophobic graphene sheet over hydrophilic atoms is also studied. Atoms interact based on the following potential: $\phi(x) = 4 \varepsilon \left\{ \left(\frac{\sigma}{r} \right)^{12} - \left(\frac{\sigma}{r} \right)^n \right\}$. The potential between Ar-Ar, Ar-Pt and Ar-Graphene is defined by Lennard-Jones 12-6 function (n=6). The interaction between hydrophilic atoms and argon atoms is governed by n=2, so that they have long range attractive force. The cut-off distance was set as 10σ . Interaction parameters are listed in Table 1 below.

Table 1: Lennard Jones potential parameters		
	ε (10^{-21} J)	σ (nm)
Ar-Ar	1.6901	0.340
Ar-Pt	1.013	0.3085
Ar-Graphene	0.81256	0.3385
Ar-Hydrophilic atom	0.34734	0.3085

Initially the simulations are run for 0.25 ns to reach equilibrium. After reaching the initial equilibrium, the upper wall is moved upward for 2 ns, with constant speed of 0.5m/s to reduce the pressure in the liquid, which helps in forming a vapor bubble. The temperature of the liquid argon is kept constant using Nose-Hoover style non-Hamiltonian thermostat. After a bubble forms, the simulation is continued for another 0.25 ns by keeping the platinum upper wall fixed, and statistical analysis is performed. The local pressure of the system is calculated by statistical averaging of principle stresses on individual atoms present in localized bins. The local density was calculated based on the number of atoms in localized bins.

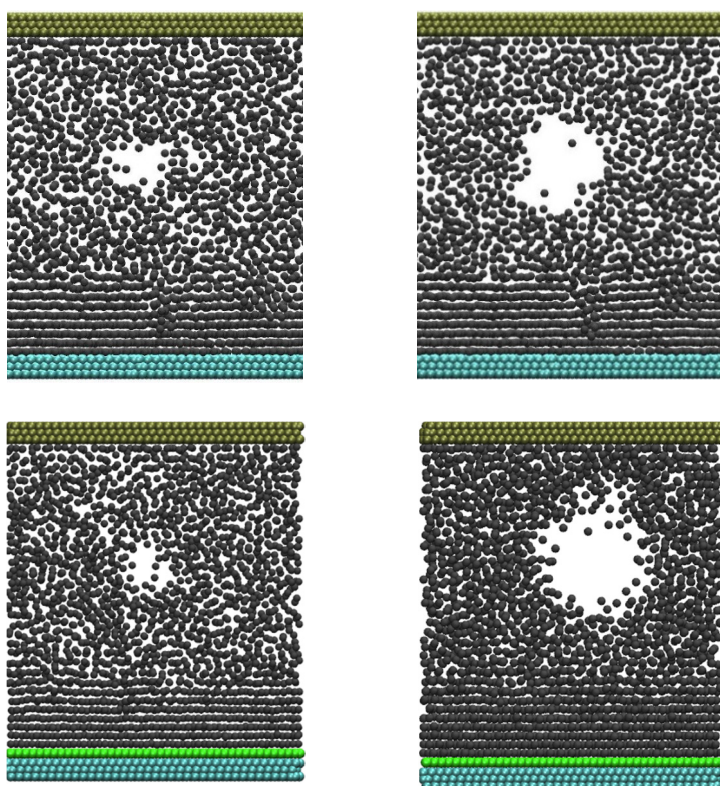


Figure S1: Molecular dynamics simulation snapshots in increasing time (left to right) of bubble nucleation on hydrophilic surface, without (upper row) and with (lower row) a hydrophobic coating.

The bubble nucleation snapshots are shown in Fig. 1 for both hydrophilic and hydrophobic surfaces. The bubble does not nucleate on the surface due to the high density of liquid resulting

from strong surface-liquid interaction. Further, the upper wall does not affect the location of nucleation as it can be seen to start at the center of the domain.

S2. Non-Polar Solid Liquid Interaction

In addition to the simulations/experiments reported in the main manuscript where solid-liquid interaction is strong and forms the thin liquid layer underneath the bubble during nucleation, we performed simulations/experiments with weak non-polar interactions between liquid and solid.

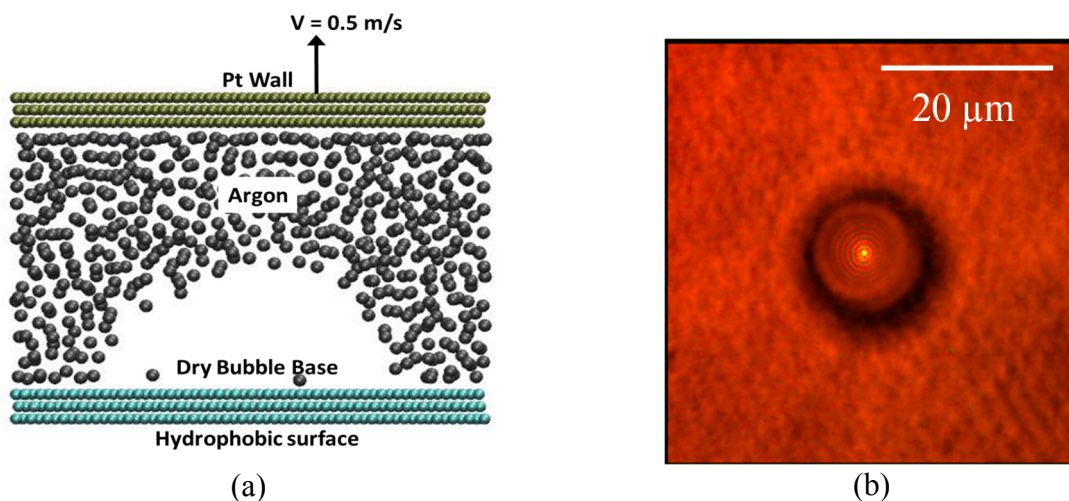


Figure S2: (a) Molecular dynamics simulation of bubble nucleation on surface with weak non-polar solid-liquid interaction, and (b) experimental image of smallest captured bubble in non-polar FC-72 liquid

In the molecular simulations, the Ar-lower wall atom interaction was changed to 12-6 with $\varepsilon = 0.534 \times 10^{-21} \text{ J}$ and $\sigma = 0.3085 \text{ nm}$. As seen in Fig. S2-a, the bubble nucleates directly on the surface with a dry base, i.e. no liquid atom layers are present underneath the bubble. Similar phenomena was also observed in experiments, where instead of water, non-polar liquid FC-72 was used. Fringes were not observed in the first captured bubble image ($\sim 10 \mu\text{m}$), showing the absence of the microlayer wetting the entire bubble base (Fig. S2-b).

S3. Estimation of Microlayer Profile & Center Curvature

The construction of the microlayer profile for an image consists of the following six steps: 1) converting the original images (Fig. S3a) to grayscale (Fig. S3b), 2) scanning the region of interest (the white line in Fig. S3c), 3) obtaining the gray intensity distribution (blue line in Fig. S3d), 4) identifying the local minimum of the intensity and its location (red dots in Fig. S3d); 5) obtaining the microlayer profile from Eq. (1) in the manuscript and applying the best curve fit (6th order least-square approximation or 6th order spline interpolation) (Fig. S3e); and 6) calculating the curvature at the center from Eq. (2) in the manuscript.

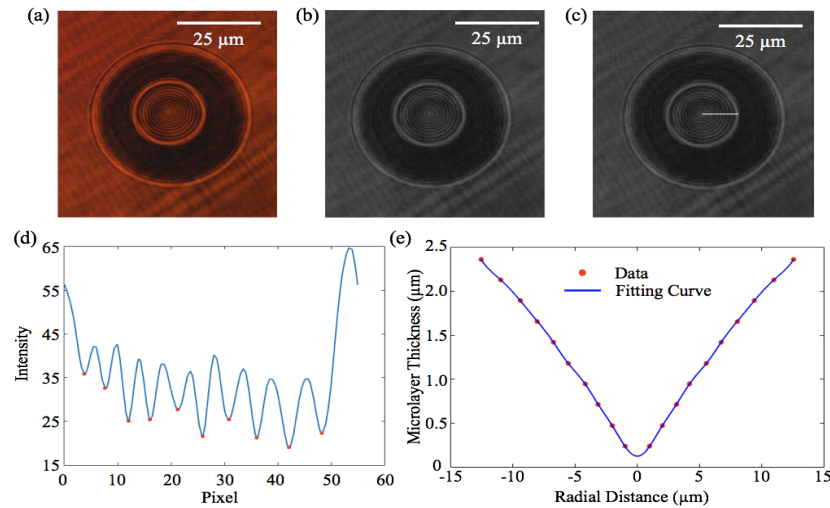


Figure S3: Image processing to obtain microlayer profile and curvature at the center.

S4. Error Analysis of Microlayer Profile

As mentioned in the main manuscript, two sets of fringes, F-1 and F-2, were observed which are independent of each other. F-1 fringes (dark thick partial rings) have decreasing fringe-gaps in the outward radial direction and are associated with interference resulting from the top curved bubble interface; while F-2 fringes are relatively closely packed and the fringe-gap increases in the outward radial direction. F-2 fringes are result of interference due to the microlayer

thin film [1]. The microlayer profile is calculated based on the location of the fringes and the relative film thickness associated to a certain fringe from Eq. 1 in main manuscript. By comparing two bubble images with different illumination source (white light for figure S4-a and red laser for figure S4-b), for a bubble with three-phase contact line, the location of contact line matches with each other with different illumination sources.

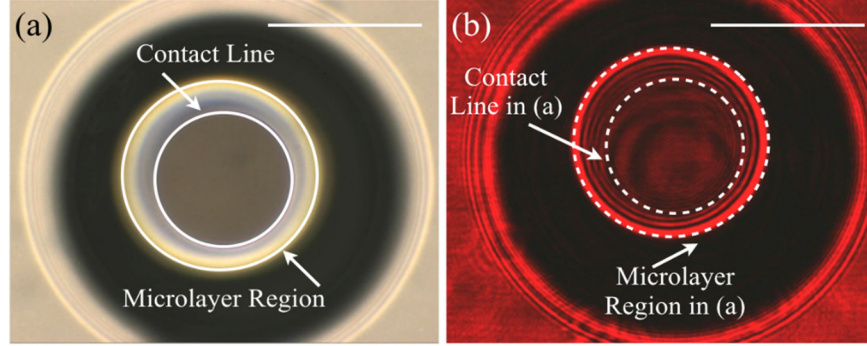


Figure S4: Bubble images with different illumination sources (a) white light and (b) red laser. The contact line and microlayer region match perfectly with these two light sources. The scale bar is 50 μm .

The incident angle was assumed as 0° when calculating film thickness using Eq. 1 in the main manuscript, while the actual incident angle is $\theta_2 - \theta_1$, as shown in Figure S5. The error from this assumption can be obtained by Eq. S1.

$$t_{err} = 100\% \times \left| \frac{\cos(0)}{\cos(\theta_2 - \theta_1)} - 1 \right| \quad \text{Eq. S1}$$

where $\theta_1 = \arcsin(x/r)$, x is the radial distance from the bubble base center to the point of interest, r is bubble radius; $\theta_2 = \arcsin(n_l/n_v \cdot \sin(\theta_1))$, n_l , n_v are index of refraction of liquid and vapor respectively. Thus, the maximum t_{err} is 1.9% for the bubble at 0.4 s (Figure 4-a1 in the main manuscript) and 1.6% for the bubble at 4 s (Figure 4-a2 in the main manuscript). In real life, the incident light for the refraction at the upper bubble interface would not be exactly vertical. For an error of $\pm 5^\circ$ in the tilted incident light, the maximum t_{err} becomes 5.7% for the bubble at 0.4 s,

and 5.0% for the bubble at 4 s. Thus, the maximum error for the film thickness would be < 5.7% for the worst case, and thus, the experimental results are reliable.

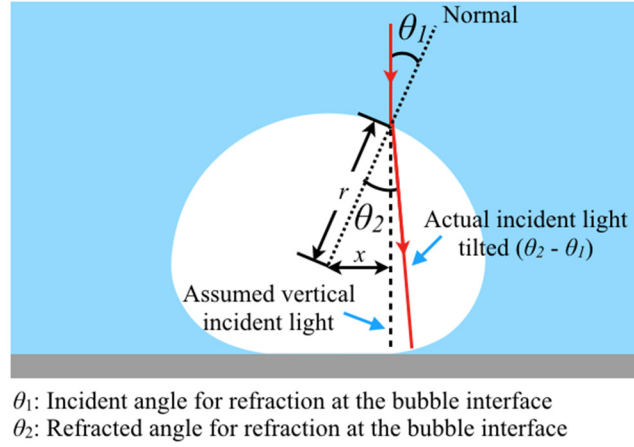


Figure S5: Tilted incident light due to the refraction occurring at the upper bubble interface.

S5. Cyclic Behavior of Curvature at Center of Microlayer

A cyclic behavior of the curvature at the bubble base center was observed (Figure 5 in the main manuscript), due to the competition between the Marangoni flow and capillary pressure driven flow. The Marangoni flow drives liquid away from the center (thus increasing curvature at the center), while the capillary driven flow drives liquid toward the center (thus decreasing curvature at the center). The time required for the curvature at the center to change depends on the competing mass flow rate between Marangoni and capillary flows.

The ratio of Marangoni flow rate to capillary flow rate is estimated based on the work [2], where Marangoni flow and capillary flow in a V-shape wedge were investigated theoretically. The data of ratio of dimensionless Marangoni flow rate to dimensionless capillary flow rate (kQ_2^*/Q_1^* , k is a geometric parameter of the channel; Q_2^* is dimensionless Marangoni flow rate; Q_1^* is dimensionless capillary flow rate) were obtained from the plot in Ref. [2] (Figure S6); and then this ratio (kQ_2^*/Q_1^*) was expressed as a function of β (half of the wedge angle, Eq. S2). This ratio

(kQ_2^*/Q_1^*) in the microlayer was estimated as 6.20×10^{-4} by substituting $\pi/2$ to Eq. S2. k is negative and in the order of 0.1, while both the right hand side of Eq. S3 and Eq. S4 are in the similar order of $10^{-12} \text{ m}^3/\text{s}$, and thus, ratio of Marangoni flow rate to capillary flow rate (Q_1/Q_2) can be in the order of 10^3 . This implies that when the capillary flow is weakest, Marangoni flow dominates and causes instantaneous decrease of film thickness most at the center. This sudden decrease in thickness relates to the sudden jump in curvature to its peak value in less than a few milliseconds as observed in our experiments.

$$k \frac{Q_2^*}{Q_1^*} = 2.623 \cdot e^{-5.316} + 1.313 \times 10^4 \cdot e^{-103.6} \quad \text{Eq. S2}$$

$$\frac{Q_1}{Q_1^*} = -\frac{d\sigma}{dT} \frac{dT}{dx} \frac{h^3}{\mu} \quad \text{Eq. S3}$$

$$\frac{Q_2}{Q_2^*} = h^4 \frac{\sigma}{\mu} \frac{d}{dx} \left(\frac{k}{h} + \frac{A_1}{h} \left(\frac{dh}{dx} \right)^2 + A_2 \frac{d^2 h}{dx^2} \right) \quad \text{Eq. S4}$$

where Q_1 and Q_2 are Marangoni flow rate and capillary flow rate respectively; σ is surface tension; T is temperature; x is the coordinate in the flow direction, h is liquid film thickness; μ is viscosity of the liquid. A_1 and A_2 are also constant depending on the wedge geometry and liquid wettability.

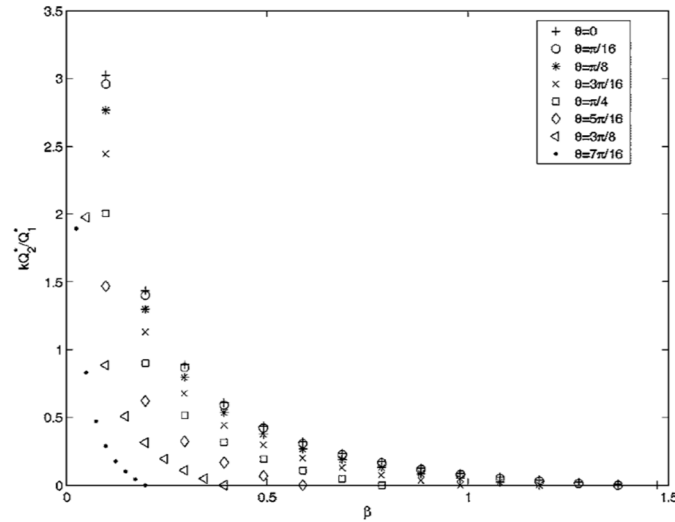


Figure S6: Ratio of dimensionless Marangoni flow rate to dimensionless capillary flow rate from Ref. [2].

The curvature at the center is also sensitive to the competition between Marangoni flow and capillary flow. Figure S7 shows a plot regarding the steady liquid profile in the wedge with different Marangoni flow and capillary flow from Ref. [2], in which D is a geometric parameter and M is modified Marangoni number $\propto Q_1^*/Q_2^*$ (i.e. larger M implies stronger Marangoni flow), and are defined as:

$$M = \frac{Q_1^*}{Q_2^*} \frac{1}{A_2 \epsilon^2} \frac{\sigma_T \Delta T_{\max}}{\sigma_o} \quad \text{Eq. S5}$$

$$D = \frac{k}{A_2 \epsilon^2} \quad \text{Eq. S6}$$

where A_2 , ϵ and k are all geometric parameters (Ref. [2]). The following analysis is done for two cases in order to study the competing effects of Marangoni and capillary on the center curvature: $D/M = 20$ and $D/M = 2$, assuming same geometric parameters for both. The microlayer thickness profiles of $D/M = 20$ and $D/M = 2$ are used from Ref. [2] to estimate the curvature. The curvature at the center increased from 0.09 ($D/M = 20$) to 0.34 ($D/M = 2$).

Comparing this analysis to our experimental observation, at the end of the each cycle (point C in Figure 5 in the main manuscript), the small curvature at center ($\sim 0.1 \mu\text{m}^{-1}$) implies weak capillary flow and is similar to the aforementioned case $D/M = 20$. Thus, at that moment, Marangoni flow dominates and the liquid flows away from the center, leading to an instantaneous sudden drop in thickness and a sudden jump in curvature to $\sim 0.35 \mu\text{m}^{-1}$ (corresponding to point A in Figure 5 in the main manuscript), i.e. the peak of the next cycle and similar to the $D/M=2$ case here.

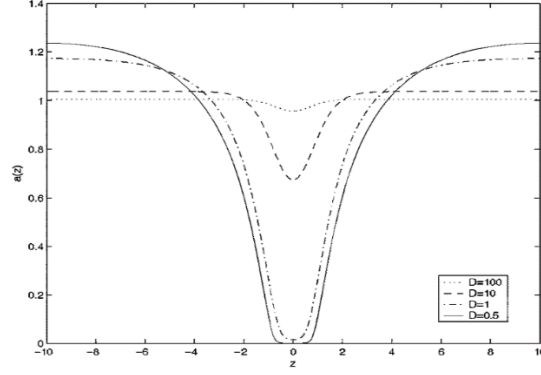


Figure S7. Steady liquid profile with different D/M for $M=5$ from Ref. [2].

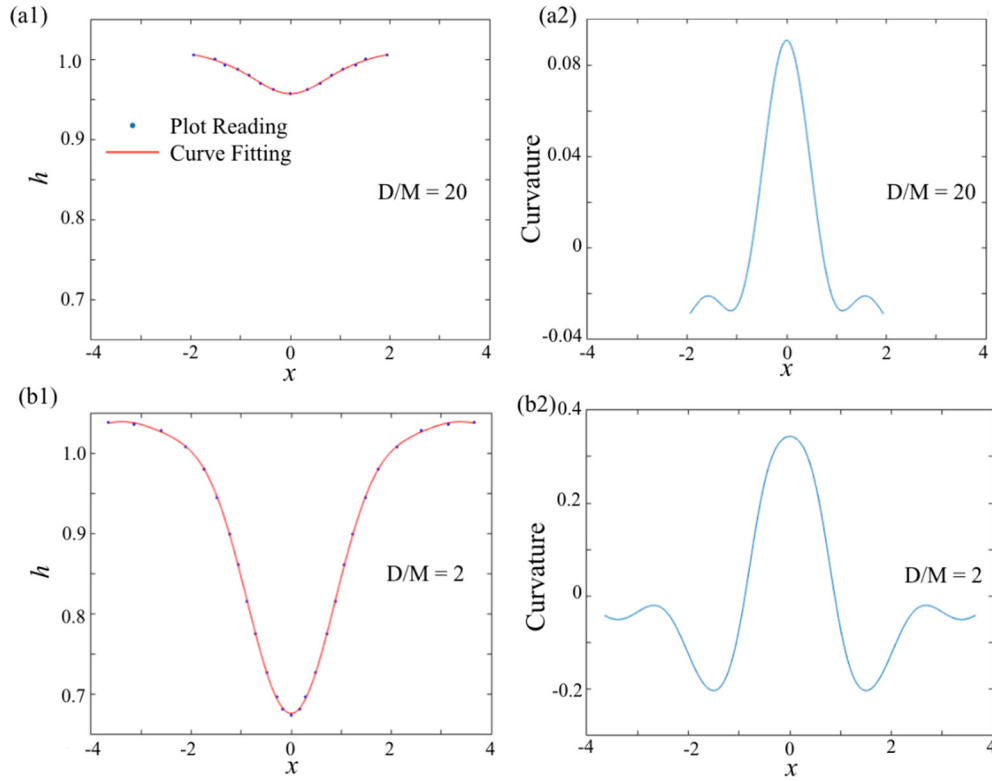


Figure S8: Microlayer thickness profile from Ref. [2] for $D/M = 20$ (a1) and $D/M = 2$ (b1); and the corresponding estimated curvature profile for $D/M = 20$ (a2) and $D/M = 2$ (b2).

S6. Water-SiO₂ vs. Ar-Hydrophilic (non-polar) Surface Interaction Energy

In experiments with water-SiO₂ combination, where polar atoms are involved, we estimate from molecular simulations that thicker high-density liquid water films will form, which can be measured in experiments (the minimum film thickness which we can measure in our experimental

setup is ~ 160 nm). Polar atoms interact as a function of r^{-1} compared to r^{-2} used in the simulations (r is the distance between two atoms), thus leading to thicker high-density liquid water films. Using LAMMPS, we simulated the energy of interaction between a water molecular and a SiO₂ surface, and compare it to the non-polar argon-hydrophilic system used in our manuscript (Fig. S9).

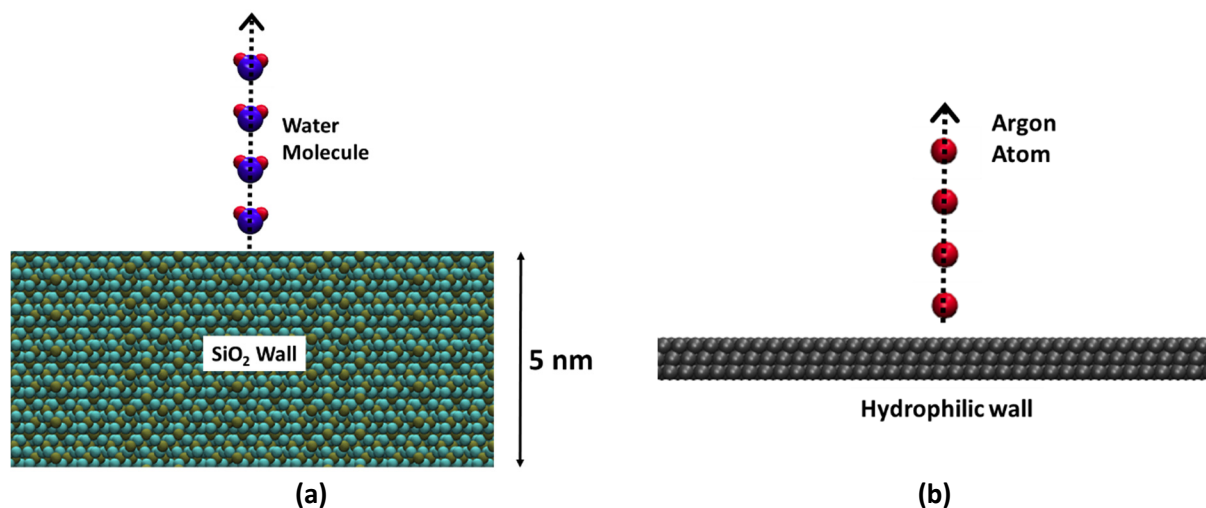


Figure S9: Molecular simulations for calculating total interaction between: (a) Silicon dioxide surface and water molecule with electrostatic interactions. (b) Non-polar interaction with argon atom and hydrophilic surface.

As SiO₂ and water molecule both have charged atoms, there exists electrostatic interaction between them which is long ranged as r^{-1} . To observe the total interaction between a SiO₂ surface and water molecule, we placed one molecule over a large SiO₂ surface (18 nm x 18nm x 5nm). Water was modeled as SPCE, while the charges on Si and O were 1.4 and -0.7 respectively; the entire system was neutral in charge. The boundaries of the domain were long enough to reduce any significant effect due to periodicity of the system. The coulomb interactions are modelled using K-Space model in LAMMPS. We moved the water molecule away from the surface and compute the potential energy as a function of distance. We performed the same analysis on the non-polar argon-hydrophilic surface used in manuscript (which interact as r^{-2}). The comparison of the energies of interaction is shown in Fig. S10. As can be seen, the water-SiO₂ interaction is much

stronger and significant even at larger distances of (50nm), thus showing that thicker water films are expected in the experiments with SiO₂ surface, and are measurable in the experiments.

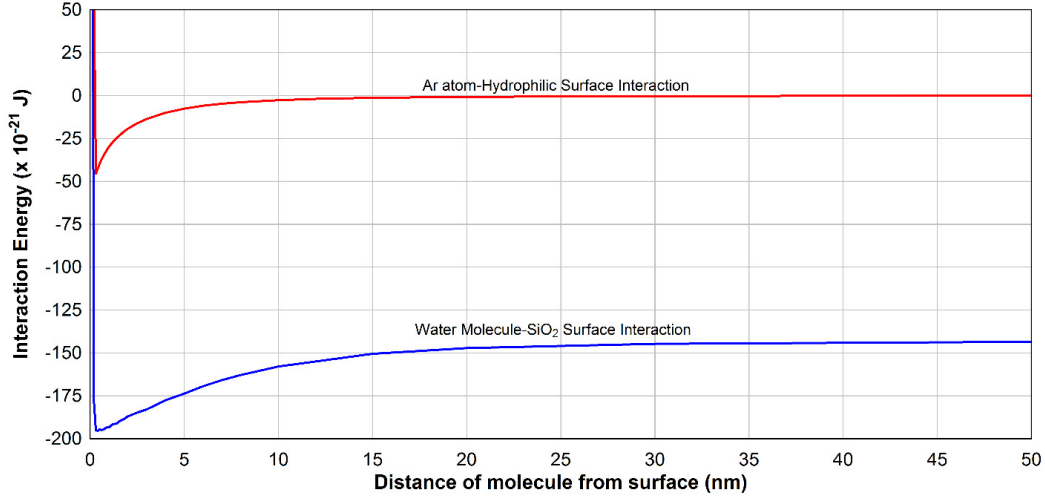


Figure S10: Comparison of interaction energy between polar water-surface combination and non-polar argon-hydrophilic surface (used in manuscript) combination.

S7. Energy for Microlayer and Contact Line Movement

The horizontal force balance at the receding or advancing contact line can be expressed as:

$$\sigma_{sv} = \sigma_{sl} + \sigma_{lv}\cos\theta_{ml} \quad \text{Eq. S7}$$

where σ_{sv} , σ_{sl} , and σ_{lv} are surface tension at the interfaces of solid-vapor, solid-liquid, and liquid-vapor, respectively; θ_{ml} represents θ_{a-ml} in advancing region and θ_{r-ml} in receding region. A net force F is generated due to the deformation of microlayer and can be obtain as:

$$F = \sigma_{lv}(\cos\theta_{a-ml} - \cos\theta_{app}) \quad \text{Eq. S8}$$

where θ_{a-ml} and θ_{app} are advancing contact angle of the pinned microlayer and apparent bubble contact angle, respectively. This net force is exerted on the contact line associated with the deformed advancing microlayer. As the y component of the local surface tension cancels out, only the projected length of contact line (L) matters in the calculation of the surface tension force. As shown in Fig. S11, L can be obtained as:

$$L = 2r_{base} \times \sin\alpha \quad \text{Eq. S9}$$

The energy required to unpin and move the contact line can be obtained as:

$$W = F \cdot L \cdot d \quad \text{Eq. S10}$$

where d is the width of the microlayer and contact line which is pinned on the surface. Combining Eqs. S8 to S10, the required energy to move the bubble can be expressed as:

$$E_{cr} = W = \sigma_{lv}(\cos\theta_{a-ML} - \cos\theta'_{a-ML}) \cdot 2r_{base}\sin\alpha \cdot d \quad \text{Eq. S11}$$

From our experimental images, the value of α is obtained to be $\sim 37^\circ$. Based on Eq. S11, we introduce a dimensionless energy E^* required to unpin and move the bubble:

$$E^* = \frac{E_{cr}}{\sigma_{lv} \cdot d \cdot d_{bubble}} \quad \text{Eq. S12}$$

Considering $d_{base} = 2r_{base} = d_{bubble}\sin\theta_{app}$ and combining Eqs. S11 and S12, the generalized form of E^* can be written as:

$$E^* = (\cos\theta_{a-ML} - \cos\theta_{app}) \sin\theta_{app} \cdot \sin\alpha \quad \text{Eq. S13}$$

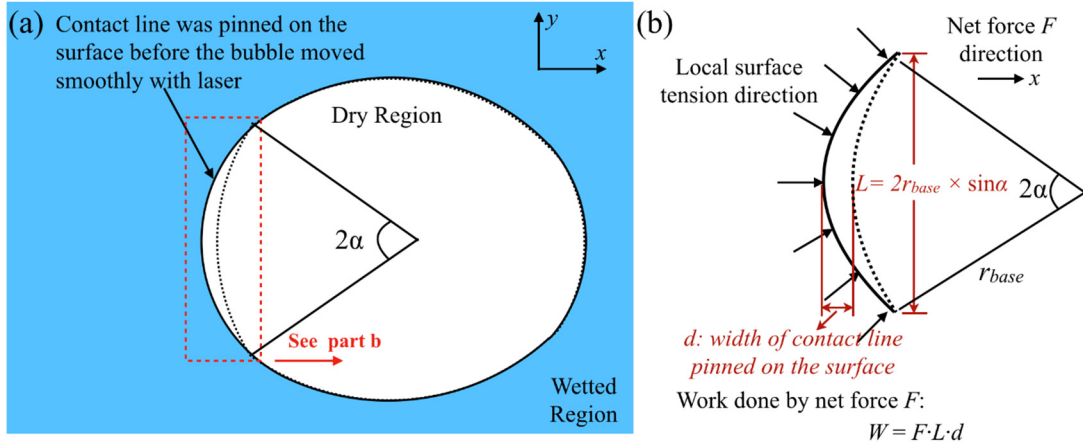


Figure S11: Schematic representing the bubble and contact line geometry for determination of the work done by the net force F .

References:

- [1] A. Zou, A. Chanana, A. Agrawal, P. C. Wayner Jr., and S. C. Maroo, Scientific Reports 6, 20240 (2016).
- [2] L. Yang and G. M. Homsy, Physics of Fluids 18, 042107 (2006).